THE JOURNAL OF
PHYSICAL CHEMISTRY B

pubs.acs.org/JPCB Article

UV–vis Photodissociation Action Spectroscopy Reveals Cytosine–Guanine Hydrogen Transfer in DNA Tetranucleotide Cation Radicals upon One-Electron Reduction

Shu R. Huang, Yue Liu, and František Tureček*

Cite This: *J. Phys. Chem. B* 2020, 124, 3505–3517 Read Online

ABSTRACT: We report the generation and spectroscopic study of hydrogen-rich DNA tetranucleotide cation radicals $(GATC+2H)^{+\bullet}$ and $(AGTC+2H)^{+\bullet}$. The radicals were generated in the gas phase by one-electron reduction of the respective dications $(GATC+2H)^{2+}$ and $(AGTC+2H)^{2+}$ and characterized by collision-induced dissociation and photodissociation tandem mass spectrometry and UV–vis photodissociation action spectroscopy. Among several absorption bands observed for $(GATC+2H)^{+\bullet}$, the bands at 340 and 450 nm were assigned to radical chromophores. Time-dependent density functional theory calculations including vibronic transitions in the visible region of the spectrum were used to provide theoretical absorption spectra of several low-energy tetranucleotide tautomers having cytosine-, adenine-, and thymine-based radical chromophores that did not match the experimental spectrum. Instead, the calculations indicated the formation of a new isomer with the 7,8-*H*-dihydroguanine cation radical moiety. The isomerization involved hydrogen migration from the cytosine N-3–H radical to the C-8 position in N-7-protonated guanine that was calculated to be 87 kJ mol^{-1} exothermic and had a low-energy transition state. Although the hydrogen migration was facilitated by the spatial proximity of the guanine and cytosine bases in the low-energy $(GATC+2H)^{+\bullet}$ intermediate formed by electron transfer, the reaction was calculated to have a large negative activation entropy. Rice–Ramsperger–Kassel–Marcus (RRKM) and transition state theory kinetic analysis indicated that the isomerization occurred rapidly in hot cation radicals produced by electron transfer with the population-weighed rate constant of $k = 8.9 \times 10^3\ s^{-1}$. The isomerization was calculated to be too slow to proceed on the experimental time scale in thermal cation radicals at 310 K.

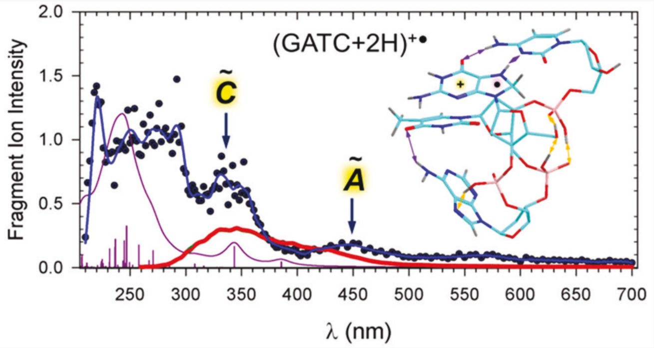

INTRODUCTION

Ionization of DNA by high-energy particles generates transient cation radicals that undergo subsequent chemical reactions.[1] Among those, reactions involving electron transfer along the DNA double strand have been investigated most frequently by experiments that focused on the kinetics and downstream analysis of radical products formed by reactions with solvent or other components in the reaction mixture.[2−6] In contrast to electron transfer, proton transfer between an ionized and neutral nucleobase has been considered to occur in guanine–cytosine (G–C) and adenine–thymine (A–T) Watson–Crick pairs. Experimental studies of oligonucleotides tagged with oxidizable groups have revealed rapid deprotonation of guanine cation radicals.[7,8] Proton transfer between base pairs has been investigated in solution[9−11] and studied *in silico* by density functional theory (DFT) calculations to indicate the proton recipient position.[12−18] In a gas-phase study of the G–C cation radical complex, O'Hair and co-workers have utilized infrared multiphoton dissociation action spectroscopy to assign the ion structure as resulting from a proton transfer between the nucleobases.[19] However, there have been few reports addressing the possibility of proton transfer along the DNA strand in cation radicals.[13]

Recently, we have generated several dinucleotide cation radicals in the gas phase and studied their structure and reactivity using UV–vis photodissociation (UVPD) action spectroscopy in combination with tandem mass spectrometry and time-dependent DFT calculations.[20−22] In our approach, the cation and radical moieties were generated on separate nucleobases in the form of the respective proton and hydrogen atom adducts. The nucleobase radicals have been found to have specific spectroscopic signatures when studied by UVPD action spectroscopy that allowed us to assign the position of

Received: February 26, 2020
Revised: April 9, 2020
Published: April 9, 2020

Scheme 1. Formation of $(GATC+2H)^{+\bullet}$

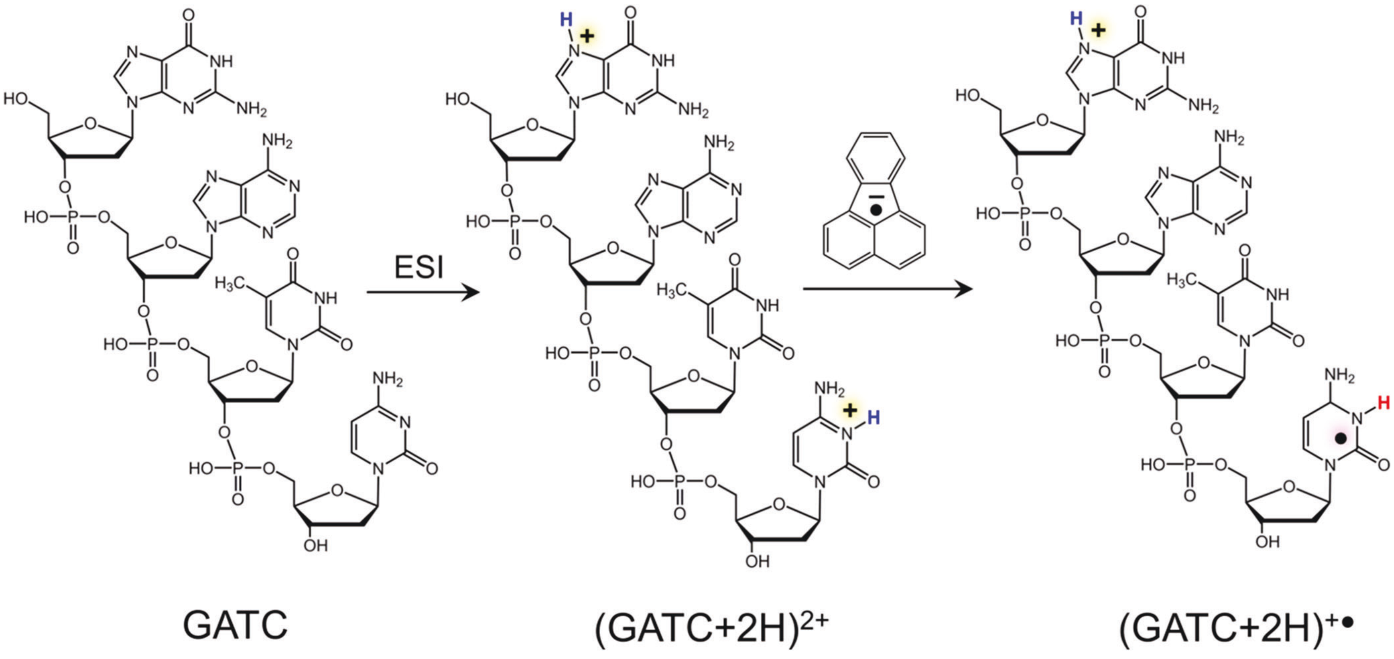

the hydrogen atom determining the radical site. One feature that has been found by our studies was interbase hydrogen atom transfer that spontaneously occurred in $(AA+2H)^{+\bullet}$ and $(GG+2H)^{+\bullet}$ dinucleotide cation radicals within milliseconds of their formation.[20,21] We observed that, while interbase hydrogen transfer from $(C+H)^{\bullet}$ to $(G+H)^{+}$ was substantially exothermic and therefore thermodynamically favored, it occurred to a different extent in dinucleotide cation radicals $(CG+2H)^{+\bullet}$ and $(GC+2H)^{+\bullet}$ because of kinetic constraints imposed by the backbone conformation.[21] This raised the question of the thermodynamics, kinetics, and mechanism of hydrogen atom migration in larger oligonucleotide cation radicals. Here, we report the generation and spectroscopic investigation of tetranucleotide cation radicals containing combinations of all four DNA nucleobases, as in $(GATC+2H)^{+\bullet}$ and $(AGTC+2H)^{+\bullet}$. We wish to show that these large and complex systems are amenable to detailed structural analysis by UV−vis action spectroscopy and electronic structure calculations.

■ EXPERIMENTAL SECTION

Materials and Methods. DNA tetranucleotides GATC and AGTC were custom-synthesized by Integrated DNA Technologies (Coralville, IA) and used as received. Mass spectra were measured on a modified Bruker amaZon Speed 3D ion trap mass spectrometer equipped with an auxiliary ion source for electron transfer dissociation (ETD) and coupled to a laser.[23] The tetranucleotides were dissolved in 50:50:1 acetonitrile−water−acetic acid at 10−20 μM concentrations and electrosprayed into the ion trap. The doubly charged ions, $(GATC+2H)^{2+}$ or $(AGTC+2H)^{2+}$, were selected by mass and subjected to one-electron reduction by ion−ion reactions with fluoranthene anion radicals at a 150 ms reaction time. The resulting cation radicals were again selected by mass in the ion trap and probed by laser photodissociation. The laser beam was provided by an EKSPLA NL301G Nd:YAG laser (Altos Photonics, Bozeman, MT, USA) working at 20 Hz frequency and 3−6 ns pulse width. The photon pulses were treated by a PG142C unit (AltosPhotonics, Bozeman, MT, USA) which incorporated a third harmonic generator and optical parametric oscillator coupled with an optional second harmonic generator to enable wavelength tuning in the range of 210−700 nm. The laser beam (6 mm diameter) exiting the PG142C unit was aligned and focused into the ion trap. The laser pulse energies were measured at each experimental wavelength using an EnergyMax-USB J-10MB energy sensor (Coherent Inc., Santa Clara, CA, USA) to calibrate the action spectra. The measured photofragment ion intensities were normalized to the number of photons per pulse.

Calculations. Precursor $(GATC+2H)^{2+}$ dication structures were obtained for 18 combinations of protomers in which protons were placed in the basic positions on different nucleobases, which were N-7 on G, N-1 or N-3 on A, O-2 or O-4 on T, and N-3 or O-2 on C. Conformation analysis of the dications was performed by Born−Oppenheimer molecular dynamics (BOMD) calculations using the semiempirical all-valence-electron PM6 method[24] supplemented with corrections for dispersion and hydrogen bonding interactions, PM6-D3H4,[25] and run by MOPAC[26] under the Cuby4 platform,[27] as described previously.[22] BOMD trajectories were run for 20 ps at 410−610 K using the Berendsen thermostat algorithm.[28] Selected low-energy conformers from the BOMD runs of each protomer were reoptimized by density functional theory (DFT) calculations using the B3LYP,[29] ωB97X-D,[30] and M06-2X[31] hybrid functionals. The B3LYP calculations of dications were performed with the 6-31G(d,p) basis set to provide harmonic frequencies that were used to calculate ion enthalpies and entropies at the ion trap temperature (310 K). The ωB97X-D and M06-2X calculations were carried out with the 6-31+G(d,p) basis set to provide the electronic terms. The combined electronic, enthalpy, and entropy terms were combined to produce free energies that were used to rank conformers of each protomer. In addition, solvation energies in water were calculated with ωB97X-D/6-31+G(d,p) using the polarizable continuum model.[32] The lowest-free-energy gas-phase ions in each group were used for the selection of protomers in the charge-reduced tetranucleotide cation radicals. Cation radical structures were optimized by B3LYP

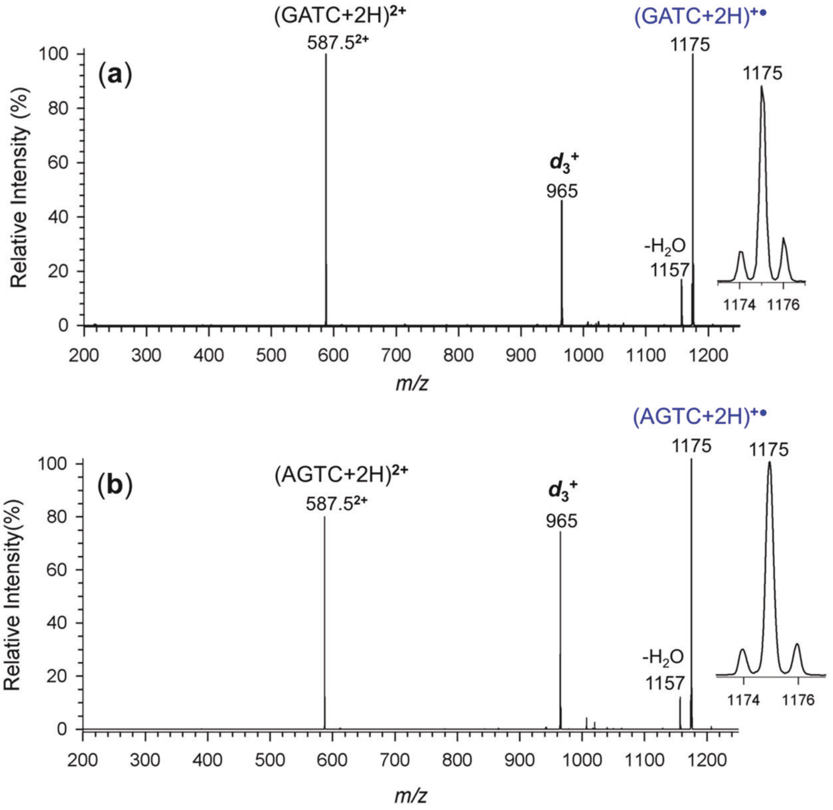

Figure 1. ETD-MS^2 spectra of (a) (GATC+2H)$^{2+}$ and (b) (AGTC+2H)$^{2+}$ ions at m/z 587.5. Insets show the charge reduced ions at m/z 1175.

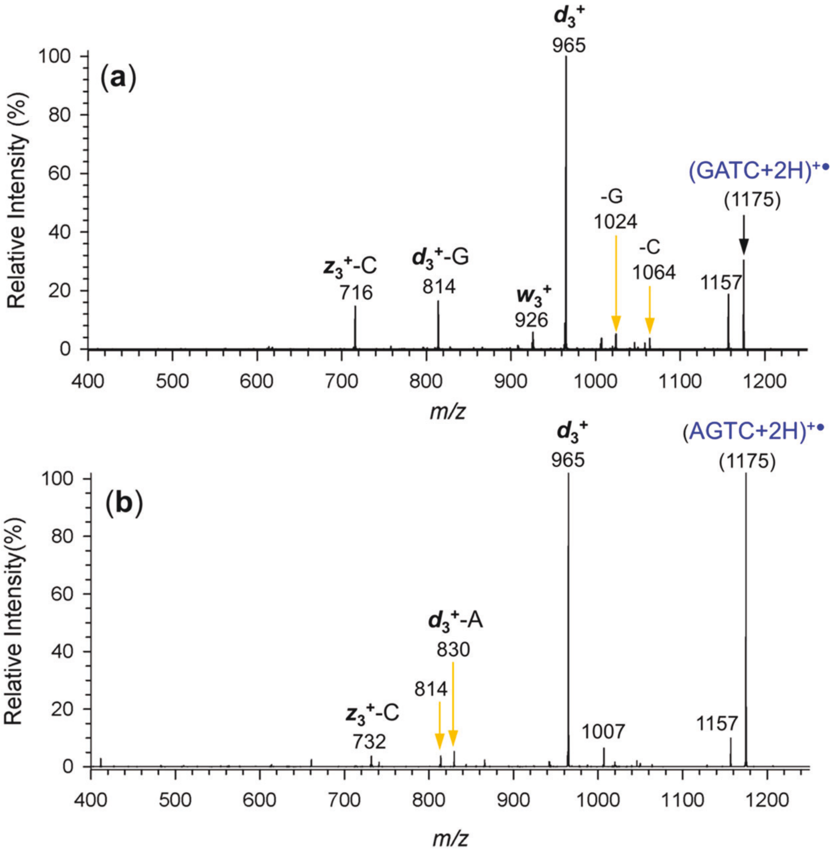

Figure 2. CID-MS^3 spectra of (a) (GATC+2H)$^{+•}$ and (b) (AGTC+2H)$^{+•}$ ions at m/z 1175.

and M06-2X calculations with the 6-31+G(d,p) basis set that were run within the spin unrestricted formalism. Single-point energies were calculated with M06-2X/6-311++G(2d,p) on the M06-2X/6-31+G(d,p) optimized geometries. Atomic spin densities were calculated using the natural population analysis[33] of the M06-2X/6-31+G(d,p) wave functions.

Based on our previous benchmarks,[34] we selected UM06-2X/6-31+G(d,p) for time-dependent DFT calculations[35] of an extensive set of vertical and vibronic transitions in the cation radicals. Vertical excitations were calculated for 90−145 excited states to probe transitions within the experimentally studied region of 210−700 nm. To calculate vibronic excitations, we used 300 Boltzmann-ranked ground-state configurations that were generated by the Newton X program[36] from the B3LYP/6-31+G(d,p) calculated harmonic normal modes of each cation radical at 310 K and submitted for TD-DFT calculations. The number of excited electronic states in these vibronic TD-DFT calculations (12−13) was chosen to include excitations with wavelengths down to ca. 270 nm, covering the structurally characteristic part of the experimental wavelength range of 210−700 nm. All of the electronic structure calculations were performed with the Gaussian 16 (revision A.03) suite of programs.[37] Rice−Ramsperger−Kassel−Marcus calculations[38] were run with a QCEP program[39] that was recompiled for Windows 7.[40] The calculations were performed in the 88−795 kJ mol^{-1} energy range with 2.092 kJ mol^{-1} (0.5 kcal mol^{-1}) steps and with a direct count of quantum states for the 387 and 386 normal modes in the reactant and transition state, respectively. Rotations were treated adiabatically, and the microcanonical k(E,J,K) rate constants were Boltzmann-averaged over the population of rotational states at 310 K. Transition state theory calculations used the standard formula with the M06-2X/6-311++G(2d,p) activation energy and partition functions based on B3LYP/6-31+G(d,p) normal-mode vibrational analysis.

■ RESULTS AND DISCUSSION

Ion Formation. Cation radicals (GATC+2H)$^{+\bullet}$ and (AGTC+2H)$^{+\bullet}$ were generated from the tetranucleotides, as shown for (GATC+2H)$^{+\bullet}$ in Scheme 1. Electrospray ionization (ESI) of the tetranucleotide solutions produced the respective dications, (GATC+2H)$^{2+}$ and (AGTC+2H)$^{2+}$, as the dominant ion species at m/z 587.5 (Figure S1a,b, Supporting Information). The dications were isolated by mass and partially reduced by electron transfer in ion−ion reactions with fluoranthene anions. These reactions yielded (GATC+2H)$^{+\bullet}$ and (AGTC+2H)$^{+\bullet}$ cation radicals at m/z 1175 as the main products (Figure 1a,b), that were accompanied by fragment ions by loss of water (m/z 1157) and backbone cleavage (m/z 965). The cation radicals were isolated by mass and interrogated by MS^3 collision-induced dissociation (CID) and UVPD spectra.

CID of both (GATC+2H)$^{+\bullet}$ and (AGTC+2H)$^{+\bullet}$ (Figure 2a,b) proceeded with elimination of the dehydrocytidine radical moiety ($C_9H_{12}N_3O_3$, 210 Da) from the 3′-terminus, producing the dominant even-electron fragment ions at m/z 965 that were also observed to form spontaneously upon electron transfer (Figure 1a,b). This dissociation was analogous to the standard backbone cleavage and formation of $\boldsymbol{d}_3$ ions upon fragmentation of even-electron nucleotide cations.[41,42] Loss of neutral 3′-cytosine (m/z 1064) and 5′-guanine (m/z 1024) nucleobases was observed as minor dissociations of (GATC+2H)$^{+\bullet}$ (Figure 2a), whereas loss of terminal nucleobases (A and C) from (AGTC+2H)$^{+\bullet}$ was negligible (Figure 2b). Consecutive dissociations of the $\boldsymbol{d}_3$ ions were investigated by further CID-MS^3 (Figure S2a,b, Supporting Information) and MS^4 (Figure S3a,b). These spectra revealed a loss of guanine (m/z 814) from both $\boldsymbol{d}_3$(GAT)$^+$ and $\boldsymbol{d}_3$(AGT)$^+$, whereas loss of adenine (m/z 830) was significant only from the 5′-position in $\boldsymbol{d}_3$(AGT)$^+$. The loss of the 5′-terminal nucleobase was followed by an elimination of the 3′-phosphoric acid, giving fragment ions at m/z 716 and 732 from $\boldsymbol{d}_3$(GAT)$^+$ and $\boldsymbol{d}_3$(AGT)$^+$, respectively. The nucleobase positions in these cations clearly affected the dissociations, with the 5′-base dissociating more readily.

Photodissociation and Action Spectra. UVPD of (GATC+2H)$^{+\bullet}$ was first investigated at 245 nm, where regular DNA[43−45] as well as DNA gas-phase ions have absorption bands.[20] The spectrum (Figure 3a) showed a dominant fragment ion at m/z 716 which we assigned to a secondary elimination of guanine and H_3PO_4 from the $\boldsymbol{d}_3$ ion. Another possibility, the isobaric $(\boldsymbol{z}_3 - \mathrm{C})^+$ ion with the same theoretical $C_{25}H_{32}N_{17}O_{14}P_2$ composition, was less likely because of the absence in the spectrum of its $\boldsymbol{z}_3$ precursor at m/z 827. The pulse-dependent measurement (inset in Figure 3a) showed a complete depletion of the (GATC+2H)$^{+\bullet}$ precursor ion after >6 laser pulses at 245 nm. The UVPD spectrum of (AGTC+2H)$^{+\bullet}$ (Figure 3b) was different, showing a dominant $\boldsymbol{d}_3$ fragment ion at m/z 965 but little further dissociation by loss of nucleobases or H_3PO_4. A prominent fragment ion at m/z 412 can be assigned to the consecutive elimination of guanine and H_3PO_4 from the $\boldsymbol{d}_2{}^+$ ion (m/z 661). The similarity of the CID and UVPD spectra is remarkable. Despite the different excitation modes and energetics, the spectra displayed the same type of dissociations that involved backbone cleavages

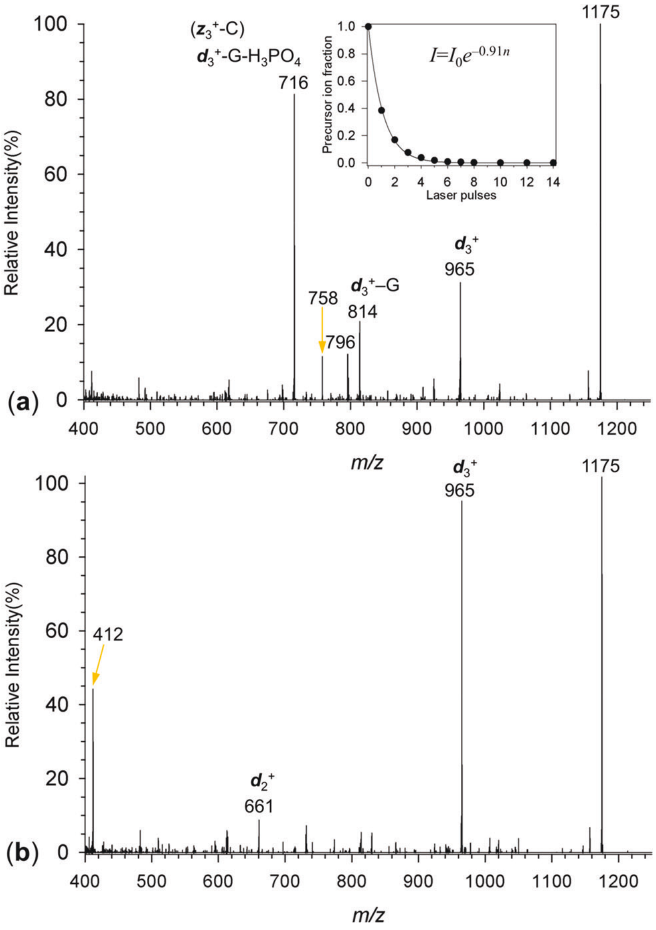

Figure 3. UVPD spectra (245 nm, two laser pulses) of (a) (GATC+2H)$^{+\bullet}$ and (b) (AGTC+2H)$^{+\bullet}$ ions at m/z 1175. The inset in part a shows the dependence of precursor ion relative intensity on the number of laser pulses.

and phosphoester eliminations. This indicated that the excited electronic states in the radicals accessed by UVPD were rapidly converted to vibrationally hot ground electronic states to drive the dissociations. This is analogous to the ultrafast internal conversion of excited electronic states in nucleobases and nucleosides, as studied in solution[46,47] and the gas phase.[48−51]

The fragment ions identified by single-wavelength UVPD were then used to monitor the action spectra of $(GATC+2H)^{+\bullet}$ and $(AGTC+2H)^{+\bullet}$ in the 210−700 nm range. The action spectrum of $(GATC+2H)^{+\bullet}$, when expressed as a sum of photofragment ion channels (Figure 4a), displayed several bands with maxima at 220, 250, 270, 290, 340, 450, and what appeared as a very weak band at 575 nm. The main contribution to the 220 nm band was from the $\boldsymbol{d}_3^{+}$ fragment ion channel (Figure 4b) that also showed maxima at 280, 340, and 450 nm. The other major channel, represented by the m/z 716 ion, showed band maxima at 220, 270, 330, and 450 nm, The m/z 814 channel, assigned as $(\boldsymbol{d}_3 - \mathrm{G})^{+}$, showed bands with maxima at 250, 300, 330, and 450 nm (Figure 4b).

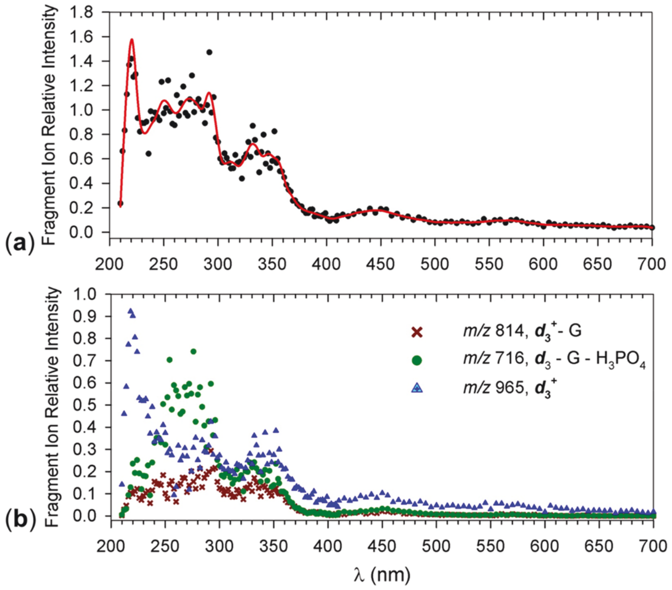

Figure 4. UVPD action spectra of $(GATC+2H)^{+\bullet}$ plotted as (a) sum of fragment ion intensities and (b) mass resolved photodissociation channels.

The action spectrum of $(AGTC+2H)^{+\bullet}$ (Figure 5a) displayed bands with maxima at 220, 255, 280, 330, and 570 nm, the last pertaining to a broad band stretching between 520 and 620 nm. The individual photofragment channels were represented by the $\boldsymbol{d}_3^{+}$ ion (m/z 965) with maxima at 220, 270, 290, 335, and 570 nm, and the m/z 412 ion appearing at 260 and 320 nm (Figure 5b). Overall, the action spectra of $(GATC+2H)^{+\bullet}$ and $(AGTC+2H)^{+\bullet}$ displayed differences in both the intensities of the bands in the visible region of the spectrum and the contributions of individual fragmentation channels to bands at 260 and 340 nm. In particular, the channels represented by consecutive dissociations, such as those of $(\boldsymbol{d}_3 - \mathrm{G})^{+}$ and $(\boldsymbol{d}_3 - \mathrm{G} - \mathrm{H_3PO_4})^{+}$, were more intense with $(GATC+2H)^{+\bullet}$.

The action spectra of $(GATC+2H)^{+\bullet}$ and $(AGTC+2H)^{+\bullet}$ were substantially different from the gas-phase absorption spectra of neutral adenine and guanine that have been reported by Clark et al. to display major bands with maxima at 252 and 274 nm, respectively.[45] The spectra of gas-phase thymine and cytosine have not been reported although calculations by Sapunar et al. have suggested absorption bands with maxima at 253 nm for thymine and 292 and 235 nm for cytosine.[43] Thus, the 250−280 nm bands in the action spectra of the cation radicals may indicate absorption by neutral nucleobases. In contrast, the long-wavelength bands at $\lambda > 300$ nm can be unequivocally assigned to radical chromophores produced by electron transfer. We also obtained reference action spectra of singly and doubly protonated GATC and AGTC (Supporting Figure S4a,b and Figure S5a,b, respectively) that were quite similar to the action spectra of dinucleotide mono- and dications reported previously.[20] In particular, the spectra of both $(GATC+2H)^{2+}$ and $(GATC+H)^{+}$ showed composite bands with maxima at 265 nm, another intense band below 210 nm, but no absorption above 300 nm (Figure S4a,b).

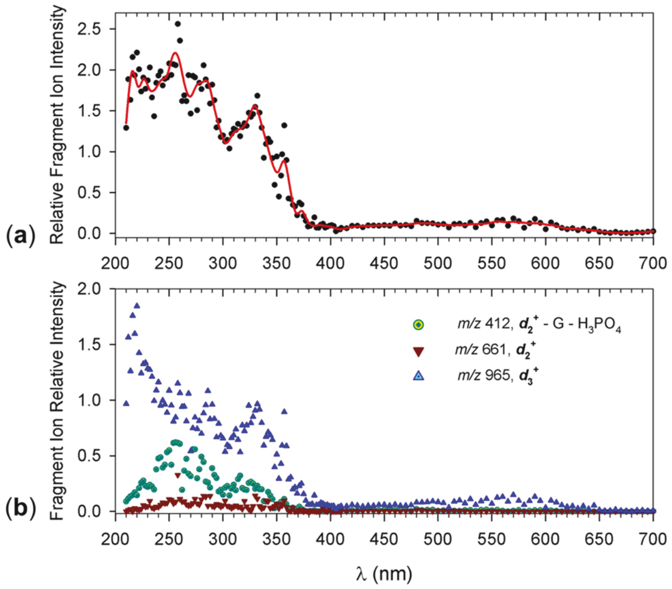

Figure 5. UVPD action spectra of $(AGTC+2H)^{+\bullet}$ plotted as (a) sum of fragment ion intensities and (b) mass resolved photodissociation channels.

Precursor Dication Structures. To interpret the action spectra of the cation radicals and assign structures, we undertook a systematic computational study of precursor dications and cation radicals produced upon one-electron reduction. First, we addressed the question of protonation sites in the tetranucleotides to assess the energetically favorable dication protomers and their conformations in the gas phase. The energetically favored protonation sites in nucleobases and nucleosides have been studied previously by experiment and theory.[51−61] The standard numbering of ring positions in DNA nucleobases is shown in Scheme 2.

Adenine is known to favor protonation at N-1, with N-3 and N-7 being the other possible protonation sites.[51,52,54,55] Guanine favors protonation at N-7 and, to a lesser extent, O-6.[52,53,56,57] Cytosine is promiscuous in that it favors protonation at N-3 and O-2 to a very similar extent.[58−61] Thymine, which is the least basic DNA nucleobase,[62] favors protonation at O-2 and O-4.[60] By combining these protonation sites for placing two protons in different nucleobases in $(GATC+2H)^{2+}$, we generated 18 theoretical protomers. These were labeled according to the proton positions; for example, G7C3 refers to the structure protonated at guanine N-7 and cytosine N-3. For each protomer, we generated several initial ad hoc conformations that were subjected to BOMD

Scheme 2. Ring-Position Numbering in DNA Nucleobases

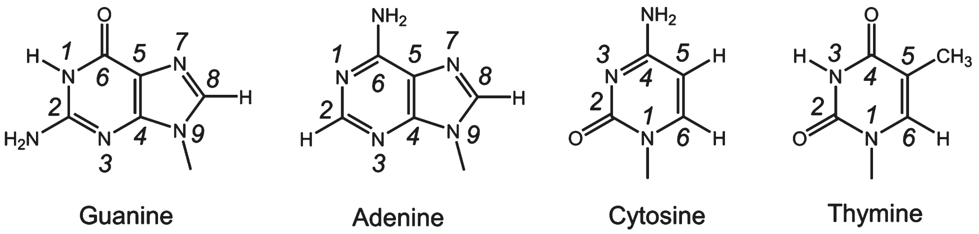

calculations yielding 20 ps trajectories at 310 K. After selecting 200 conformers at 100 fs intervals from each trajectory, the structures were fully gradient-optimized with the goal of identifying the lowest energy conformers. Selected low-energy structures from this round of geometry optimizations were further reoptimized with B3LYP to provide harmonic frequencies and identify local energy minima. One hundred B3LYP structures were used for the final rounds of optimizations that were performed with ωB97X-D and M06-2X and the 6-31+G(d,p) basis set. Single-point M06-2X energies and ωB97X-D solvation energies in water were also obtained, and the dications were ranked by free energy (Table 1). The M06-2X/6-311++G(2d,p) relative energies are discussed in the text. The Table 1 data indicated that the energetically favored protonation motifs in the order of increasing free energies were G7C3, G7A1, G7A3, A1C2, A1C3, and A3C2 that had at least one conformer within 30 kJ mol^{-1} of the G7C3 global minimum. The structures of the lowest-energy conformers of each protonation motif are shown in Figure 6. Since the dications were formed by protonation in electrospray microdroplets and then transferred to the gas phase containing the solvent vapor, relative free energies in both solution and the gas phase can play a role in determining the tautomer formation.

Table 1. Relative Free Energies of $(\mathrm{GATC+2H})^{2+}$ Dications

	relative free energy[a,b]		
ion	ωB97X-D[c]	M06-2X[d]	ωB97X-D(aq)[e]
G7C3a	0	0	0
G7A1a	12	0.2	37
G7A3	26	10	22
A1C2	44	13	66
A1C3a	18	17	22
G7C3b	29	24	42
G7A1b	29	26	50
A3C2a	46	29	22
A1C3b	43	30	3
A3C2b	49	36	22

[a] In kJ mol^{-1}. [b] Including B3LYP/6-31G(d,p) zero-point energies and 310 K enthalpies and entropies. [c] Based on ωB97X-D/6-31+G(d,p) optimized structures. [d] Based on M06-2X/6-31+G(d,p) optimized structures. [e] Including polarizable continuum model solvation energies in water dielectric.

The lowest free-energy dication structure in both the gas phase and aqueous environment (**G7C3a**) had a zwitterionic structure in which a phosphoester proton moved to the adenine N-3 position (Figure 6). This structure showed two very short hydrogen bonds, one at 1.436 Å for adenine N3−H···O−P and the other at 1.471 Å for guanine N7−H···O−P. In contrast, the only internucleobase hydrogen bond in **G7C3a** was between C−N3−H and T−O2. The ωB97X-D-optimized structure of **G7C3a** (Figure S6, Supporting Information) showed slightly longer N3−H···O−P and N7−H···O−P H-bonds but overall was very similar to that from M06-2X. This indicated that the tight H-bonding of 5′-guanine to the phosphate and the 3′-OH contributed to a folded structure in which the guanine and cytosine nucleobases were in proximity. Such a folding of nucleotide dications, as presented by **G7C3a**, is unprecedented. For example, low-energy conformers of $(\mathrm{GC+2H})^{2+}$ and $(\mathrm{CG+2H})^{2+}$ have been found to prefer extended structures, minimizing Coulomb repulsion between the charged nucleobases. Evidently, increasing both the size of the dication and the number of intramolecular hydrogen bonds in tetranucleotides overcomes charge repulsion interactions to allow low-energy folded structures to develop.

The pairing of the formally distant protonated 5′-G and neutral 3′-C was also indicated for the second lowest energy gas-phase structure **G7A1a** (Figure 6). This ion showed two G−C hydrogen bonds, and the conformation was further buttressed by H bonding between the adjacent A and T, resulting in separated G−C and A−T pairs. Hydrogen bonding between protonated and neutral nucleobases occurred to various extents in the other low-energy dication isomers. Strong G−C hydrogen bonds were found in structures **G7A3**, **A1C2**, **A1C3a**, **G7A1b**, **A1C3b**, and **A3C2b**. Structure **A1C3b**, which was substantially stabilized by solvation in water, showed G−T and C−T hydrogen bonds, whereas the protonated adenine ring was not internally solvated. Other combinations of internucleobase hydrogen bonding were G−A and C−T in **G7C3b** and G−T in **A3C2a** (Figure 6).

Cation Radical Structures Following Electron Attachment. The structures of low-energy dications served as starting points for the geometry optimization and conformational analysis of cation radicals. Attachment of an electron to $(\mathrm{GATC+2H})^{2+}$ dications of the G7C3 type resulted in several cation radicals from which we selected two lowest-energy conformers, **G7rC3a** and **G7rC3b** (Figure 7, Table 2). Radical **G7rC3a** had a high spin density in the reduced cytosine ring, as indicated by the calculated NPA spin populations.[33] Interestingly, the structural features that were characteristic of the precursor dication (**G7C3a**), which were the G−C hydrogen bonds and the A-N-3−H$^+$···$^-$O−P zwitterion dipole, were largely conserved in **G7rC3a**. In contrast, electron attachment leading to **G7rC3b** triggered substantial conformation changes. This cation radical also had a reduced cytosine ring, which, however, was not H-bonded to the other nucleobases. Instead, **G7rC3b** developed hydrogen bonds between the protonated guanine and neutral thymine and adenine bases, resulting in a globular conformation (Figure 7) that was disfavored against **G7rC3a** by low entropy.

The low-energy cation radical produced from dications of the G7A1 type (**G7A1rT**) had a more unusual structure, showing a radical site in a thymine hydrogen adduct (Figure 8). This was likely created by intramolecular proton transfer

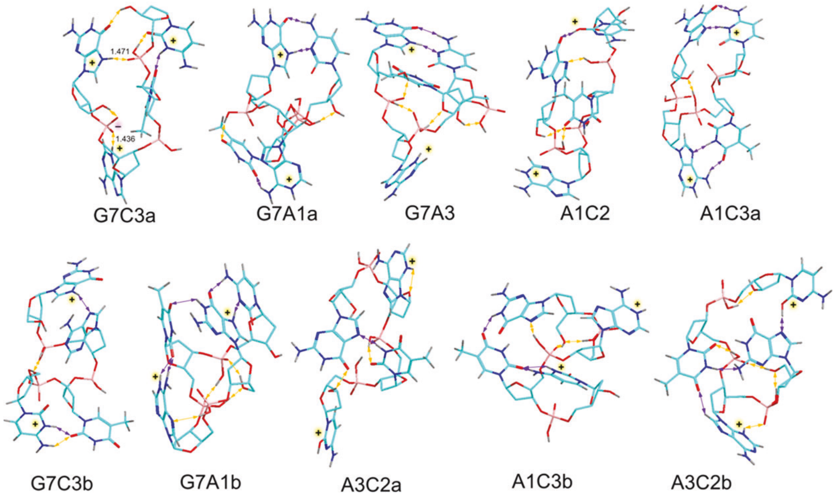

Figure 6. M06-2X optimized structures of low-energy $(GATC+2H)^{2+}$ ions. The atom color coding is as follows: cyan = C, blue = N, red = O, bronze = P, gray = H. The deoxyribose hydrogen atoms are not shown. Hydrogen bonds are indicated by double-headed arrows, purple for those between the nucleobases and yellow for the others.

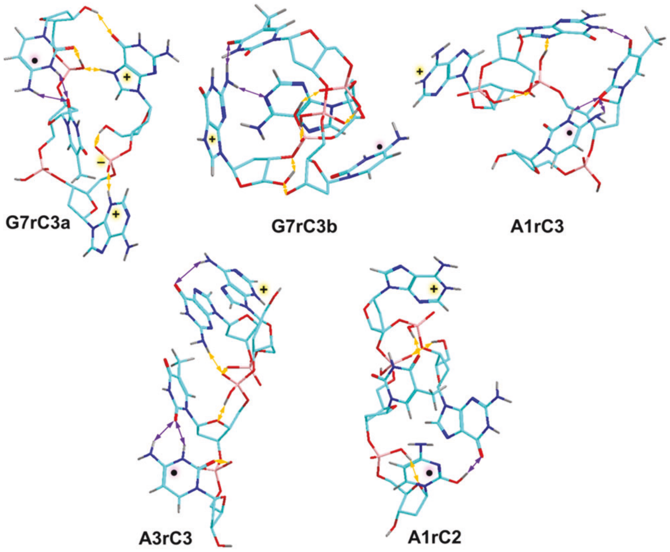

Figure 7. M06-2X optimized structures of low-energy cytosine-based radicals. The atom color coding is as in Figure 6.

from G-N-7−H to an intermediate thymine anion radical formed by electron capture. Related zwitterionic intermediates with protonated G and A and anion-radical T were obtained as local energy minima but were at substantially higher energies than **G7A1rT**. Cation radical **G7A1rT** displayed a large number of internucleobase hydrogen bonds, resulting in a globular structure of low entropy.

Electron attachment to dications of the G7A3 type produced adenine radicals with only minor changes of the conformation relative to the precursor dication G7A3, as illustrated with **G7rA3** (Figure 8), which was the lowest-energy conformer in this group. Reduction of dications of the A1C2, A1C3, and A3C3 type yielded cytosine radicals, as illustrated by the respective lowest-energy conformers within each group, **A1rC2**, **A1rC3**, and **A3rC3** (Figure 7). Finally, reduction of A3C2 dications placed the electron in the adenine ring in low-energy cation radicals such as **rA3C2** (Figure 8). Overall, the cation radicals of different protonation types showed a larger spread of relative energies than did the respective dications.

Table 2. Relative Free Energies of $(GATC+2H)^{+\bullet}$ Cation Radicals

	relative energy[a,b]	
ion[c]	radical sites[d]	M06-2X[e,f]
G7rC3a	C4,6	0 (0)
G7rC3b	C4,6	3 (16)
G7A1rT	T4,6	8 (35)
G7rA3	A2,6	45 (49)
A1rC3	C4,6	45 (49)
A3rC3	C4,6	55 (55)
rA3C2	A2,6	74 (70)
A1rC2	C4,6	91 (93)
G7rA8	A2,6,9	−72 (−55)
rG78a	G7,5,9	−87 (−72)
rG78b	G7,5,9	−51 (−29)
G7rC3a → $\mathbf{TS_{mig}}$		68
rG78a → $d_3^+ + w_1^\bullet$		159 (75)
rG78a → $d_3^+ + w_1'^\bullet$		132 (47)

[a] In kJ mol^{-1}. [b] Including B3LYP/6-31+G(d,p) zero-point energies and referring to 0 K. [c] rA, rC, rG, and rT refer to the nucleobase harboring the additional hydrogen atom at the indicated ring position. [d] Sites of highest atomic spin densities in nucleobases. [e] Single-point M06-2X/6-311++G(2d,p) energies on M06-2X/6-31+G(d,p) optimized structures. [f] Relative free energies at 310 K in parentheses.

To assign the experimental action spectrum of $(GATC+2H)^{+\bullet}$, we first obtained electronic excitation energies and absorption band intensities for 60−100 excited states of low-energy $(GATC+2H)^{+\bullet}$ cation radicals to cover the experimental wavelength range down to below 210 nm. The excited states were calculated by TD-DFT M06-2X/6-31+G(d,p) that we have previously benchmarked on equation-of-motion coupled cluster calculations of nucleobase cation radicals.[34] The calculated spectra of all of the cytosine-based radicals (**G7rC3a**, **G7rC3b**, **A1rC3**, **A3rC3**, and **A1rC2** (Figure S7a−e, Supporting Information) as well as the thymine-based radical **G7A1rT** (Figure S7f) showed very weak bands at $\lambda >$ 300 nm that were incompatible with the action spectrum of $(GATC+2H)^{+\bullet}$. The adenine-based radicals **G7rA3** and **rA3C2** showed weak bands in the 480−560 nm interval (Figure S7g,h) but again no significant absorption in the 300−

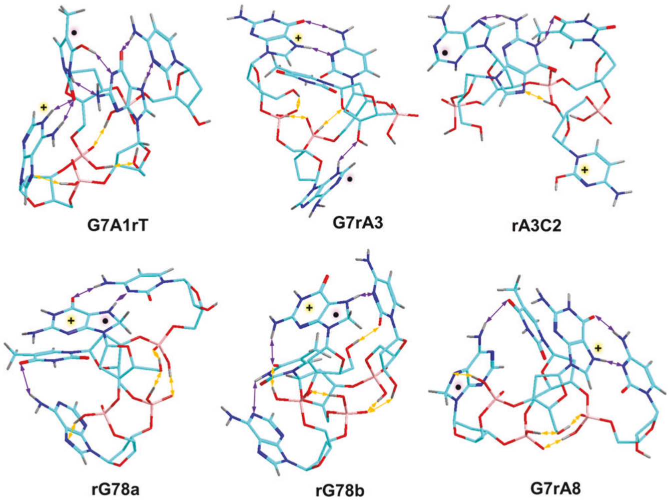

Figure 8. M06-2X optimized structures of low-energy thymine-, adenine-, and guanine-based radicals. The atom color coding is as in Figure 6.

380 nm range that could match the band in the action spectrum. The calculated electronic transitions are summarized in Supporting Tables S1−S11.

Cytosine−Guanine Isomerization. The above-described results indicated that the GATC cation radicals did not retain the expected primary cytosine or adenine radical units after being generated by electron transfer to the protonated nucleobases. To interpret the experimental data, we considered other chromophores formed by isomerization of the lowest-energy charge-reduced structures. Cation radical **G7rC3a** had a close interaction between the protonated guanine and radical-carrying cytosine rings that led to a low-energy transition state (TS_{mig}) for cytosine N-3−H migration to the C-8 position in guanine (Scheme 3). The optimized geometry of TS_{mig} indicated that it was an early transition state that was only 68 kJ mol^{-1} above the **G7rC3a** reactant (Table 2). The isomerization was exothermic (ΔH_0 = −87 kJ mol^{-1}, Table 2), yielding 7,8-dihydroguanine cation radical **rG78a** (Scheme 3). Another dihydroguanine cation radical conformer of ΔH_0 = −51 kJ mol^{-1} (**rG78b**, Table 2) could also be formed exothermically from **G7rC3a**. It is noteworthy that the isomerization within the G−C system also resulted in a proton transfer from adenine N-3−H to the proximate phosphate anion, collapsing the zwitterion and reforming the neutral adenine base (Scheme 3). An alternative isomerization of **G7rC3b** by cytosine hydrogen migration to adenine C-8 was also substantially exothermic to form radical **G7rA8** (ΔH_0 = −72 kJ mol^{-1}, Table 2). However, an interaction between the 3′-terminal cytosine and internal adenine rings to allow N-3−H atom migration would require a substantial reorganization of the ion conformation to reach the transition state. In particular, the TS for the H-migration favored a near linear arrangement of the involved C-8···H···N-3 atoms which was 154° in TS_{mig} (Scheme 3). Such an arrangement was difficult to achieve for the C → A migration where it was expected to result in an interruption of multiple hydrogen bonds in **G7rC3b**, which would be associated with a substantial increase of potential energy and a higher-energy transition state.

TD-DFT absorption spectra were calculated for **rG78a**, **rG78b**, and **G7rA8**, including vibronic transitions for 12−13 excited states (Figure 9a−c). The limited number of excited states in these calculations was dictated by the large number of vibrational configurations (300) in the ground-state cation radicals to be considered for TD-DFT vertical excitations in these rather large open-shell systems of 1773 basis functions (2964 primitive gaussians). All three spectra showed transitions in the 300−400 nm region that were vibronically broadened beyond 450 nm for **rG78a** and **G7rA8**, and even beyond 550 nm for **rG78b**. The effect on the vibronic spectra of the ion conformation in **rG78a** and **rG78b** was remarkable, and it can be attributed to an enhancement of transition moments to the dark ***B*** (for **rG78a**) and ***B*** and ***C*** (for **rG78b**) states in thermal ions (Supporting Tables S9−S11). The low (***A***−***D***) excited states corresponded to $\pi \rightarrow \pi^*$ transitions within the dihydroguanine moiety, as shown for **rG78a** (Figure 10). No G → T* charge-transfer excitation was indicated for the low excited states that could have been facilitated by the thymine proximity and electron affinity.[62] This can be explained by the unfavorable orientation of the interacting dipoles that are nearly perpendicular due to the position of the guanine and thymine rings in **rG78a** (Scheme 3). On the basis of spectra match and isomerization feasibility, we assigned **rG78a** as the dominant component of $(GATC+2H)^{+\bullet}$ cation radicals produced by electron transfer.

Energetics and Kinetics of $(GATC+2H)^{+\bullet}$ Formation. The observation of nondissociating cation radicals upon

Scheme 3. Isomerization of $(GATC+2H)^{+\bullet}$ Cation Radicals

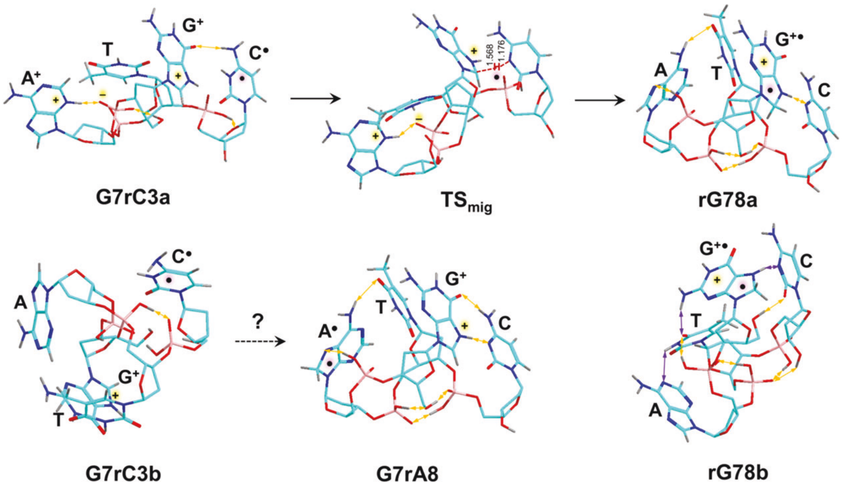

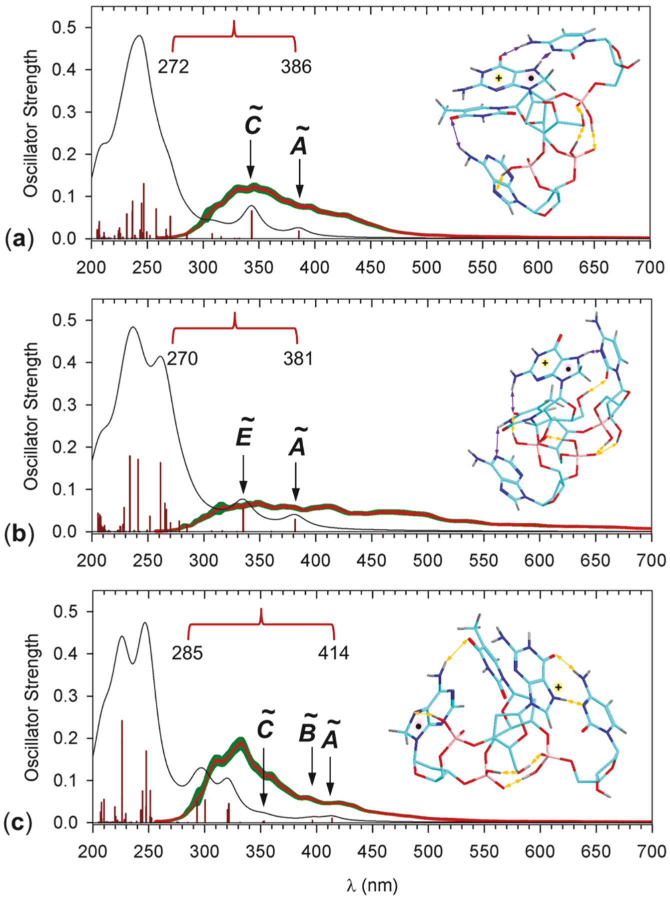

Figure 9. M06-2X/6-31+G(d,p) TD-DFT spectra and optimized structures of (a) **rG78a**, (b) **rG78b**, and (c) **G7rA8**. The black-line band shapes are from artificial broadening of the calculated excitation lines by convolution with Lorentzian peak shapes at 10 nm full width at half-maximum. The red-line band shapes are from 300 vibronic calculations of 12−13 excited states in the wavelength range shown by brackets. Green bars show the errors in the calculated oscillator strength.

electron-transfer reduction of $(\mathrm{GATC{+}2H})^{2+}$ and $(\mathrm{AGTC{+}2H})^{2+}$ raised the question of the electron transfer energetics and the cation radical stability. Previous studies of DNA dinucleotides and RNA dinucleotide chimeras have reported extensive dissociation of cation radicals upon electron transfer.[20,21] In contrast, hexanucleotide cation radicals have been reported to be stable when produced by electron transfer to the corresponding dications.[63] The energetics of the cation radical formation was evaluated from the enthalpies of the ion−ion reactions for $(\mathrm{GATC{+}2H})^{2+}$ (eq 1):

$$(\mathrm{GATC{+}2H})^{2+} + \mathrm{fluoranthene}^{-\bullet} \rightarrow (\mathrm{GATC{+}2H})^{+\bullet} + \mathrm{fluoranthene} \qquad (1)$$

A previous study of the electron transfer energetics concluded that electron detachment from the anion forms the fluoranthene molecule in its ground (S_0) electronic state.[64] Thus, the energy balance in eq 1 (ΔH_{rxn}) can be expressed by the enthalpy terms for the ground states of the reactants and products, according to eq 2, where ΔH_{f} are the pertinent enthalpies of formation at the experimental temperature, RE < 0 is the adiabatic recombination energy of $(\mathrm{GATC{+}2H})^{+\bullet}$, and EA > 0 is the electron affinity of fluoranthene.[64]

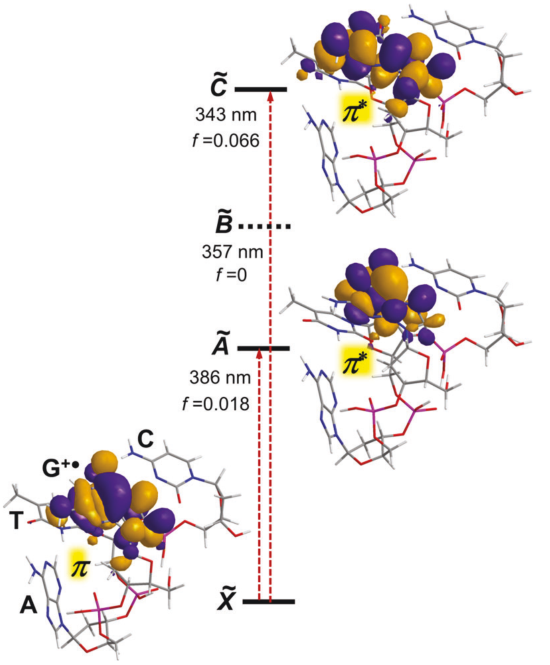

Figure 10. M06-2X/6-31+G(d,p) molecular orbitals representing the ground (X) and low excited electronic states in **G78ra**. Excitation wavelengths and oscillator strengths (f) are also shown.

$$\begin{aligned}\Delta H_{\mathrm{rxn}} &= \Delta H_{\mathrm{f}}(\mathrm{fluoranthene}) + \Delta H_{\mathrm{f}}(\mathrm{GATC{+}2H})^{+\bullet} \\ &\quad - \Delta H_{\mathrm{f}}(\mathrm{fluoranthene})^{-\bullet} - \Delta H_{\mathrm{f}}(\mathrm{GATC{+}2H})^{2+} \\ &= \mathrm{RE}(\mathrm{GATC{+}2H})^{+\bullet} + \mathrm{EA}(\mathrm{fluoranthene}) \qquad (2)\end{aligned}$$

The $\mathrm{RE}(\mathrm{GATC{+}2H})^{+\bullet}$ was calculated as −562 kJ mol^{-1}, which was combined with the calculated EA(fluoranthene) = 82 kJ mol^{-1} to give $\Delta H_{\mathrm{rxn}} = -486$ kJ mol^{-1}. Note that, in this estimate, we used the calculated EA(fluoranthene) rather than the reported experimental value (61 kJ mol^{-1})[65] in an effort to in part compensate the inaccuracies of DFT calculated energies. The ΔH_{rxn} is partitioned between the reaction products to increase their internal energy. We presumed that the partitioning proceeded by the relative vibrational and rotational heat capacities in $(\mathrm{GATC{+}2H})^{+\bullet}$ (68.5 J mol^{-1} K^{-1}) and fluoranthene (10.6 J mol^{-1} K^{-1}), providing an initial vibrational excitation in $(\mathrm{GATC{+}2H})^{+\bullet}$ as $\Delta E_{\mathrm{ET}} = 486 \times 68.5/(68.5 + 10.6) = 412$ kJ mol^{-1} (Figure 11). The total energy of $(\mathrm{GATC{+}2H})^{+\bullet}$ was then obtained as a convolution of the ET excitation energy and the internal (vibrational) energy distribution in the $(\mathrm{GATC{+}2H})^{2+}$ precursor dication that was based on the vibrational state count at 310 K. This gave the maximum of the internal energy distribution in $(\mathrm{GATC{+}2H})^{+\bullet}$ formed by electron transfer as $E_{\mathrm{max}} = 604$ kJ mol^{-1} with the distribution shown in Figure 11.

The internal energy distribution was used to calculate the distribution-weighed RRKM rate constant (k_{isom}) for the exothermic isomerization of **G7rC3a** to **rG78a** (eq 3), where $k(E)$ is the RRKM rate constant. The calculated RRKM rate constants are shown in Figure 11.

$$k_{\mathrm{isom}} = \int_{E_{\mathrm{TS}}}^{\infty} k(E)P(E)\,\mathrm{d}E \qquad (3)$$

Using the shifted $P(E)$ function from Figure 11, one obtains $k_{\mathrm{isom}} = 8.9 \times 10^{3}$ s^{-1}, indicating >99% isomerization within 1 ms and a complete isomerization on the experimental time

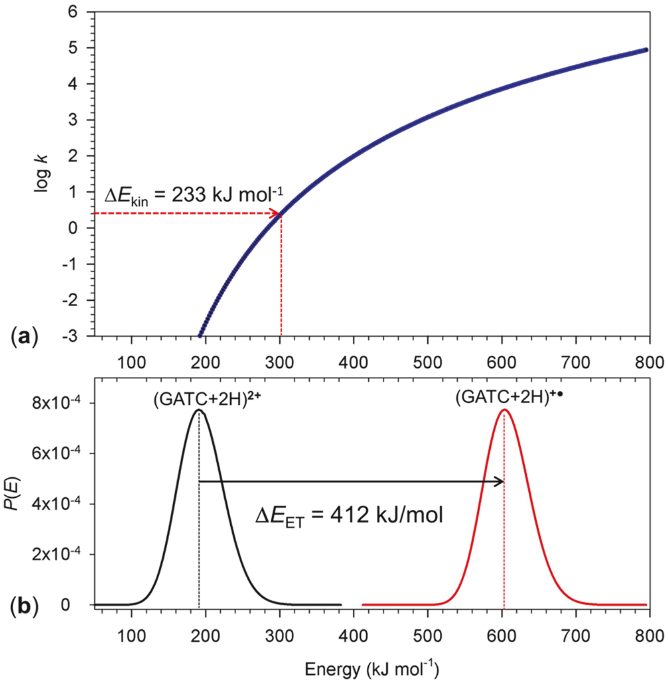

Figure 11. Top panel: RRKM rate constants for the **G7rC3a** → **rG78a** isomerization. Bottom panel: calculated vibrational energy distributions in the **G7C3a** dication at 310 K and **G7rC3a** after electron transfer.

scale of 150 ms. However, because of the He buffer gas in the ion trap, the hot ions formed by ET are expected to undergo collisional cooling that can be expressed as a competitive first order process[64] (eqs 4–7) where in brackets are the time-dependent mole fractions and k_{cool} is the cooling rate constant.

$$-\frac{[\text{G7rC3a}]_{\text{hot}}}{\text{d}t} = -(k_{\text{isom}} + k_{\text{cool}})[\text{G7rC3a}]_{\text{hot}} \quad (4)$$

$$\frac{\text{d}[\text{rG78a}]}{\text{d}t} = k_{\text{isom}}[\text{G7rC3a}]_{\text{hot}} \quad (5)$$

$$\frac{\text{d}[\text{G7rC3a}]_{\text{cool}}}{\text{d}t} = k_{\text{cool}}[\text{G7rC3a}]_{\text{hot}} \quad (6)$$

$$x(\text{G7rC3a}) = [\text{G7rC3a}]_{\text{hot}} + [\text{G7rC3a}]_{\text{cool}} \quad (7)$$

Solution of eqs 4–6 gave the mole fraction of isomerized **rG78a**, as shown in eq 8:

$$x_{\text{rG78a}} = \int_{E_{\text{TS}}}^{\infty} \frac{k_{\text{isom}}(E)}{k_{\text{isom}}(E) + k_{\text{cool}}}\{1 - \text{e}^{-(k_{\text{isom}}(E)+k_{\text{cool}})t}\}P(E)\,\text{d}E \quad (8)$$

Since we do not know the energy dependence of the cooling rate, we considered a typical range of 100–500 s^{-1}.[64] According to eq 8, this gave $x_{\mathbf{rG78a}}$ = 0.986–0.935, indicating that >93% of the primary (GATC+2H)$^{+\bullet}$ radicals can be expected to isomerize to the more stable **rG78a**. In contrast, following thermalization to 310 K, the calculated transition-state-theory rate constant (k_{therm} = 0.049 s^{-1}) would allow only 0.7% isomerization on the 150 ms time scale of the measurement (Supporting Table S12). The isomerization was substantially slowed down by a negative entropy change in the TS, $\Delta S_{\text{TS}} = -49.5$ J mol^{-1} K^{-1} at 310 K. Likewise, RRKM calculations for k_{isom}, when averaged over the vibration state distribution in **G7rC3a** at 310 K (k_{isom} = 0.031 s^{-1}), indicated negligible (0.5%) isomerization. These results strongly suggested that the isomerization was driven by vibrational excitation acquired upon electron transfer.

The threshold energy for the dissociation of **rG78r** to the $\boldsymbol{d_3}$ fragment ion and the dehydrocytidine radical $\boldsymbol{w_1}^\bullet$ (Scheme 4) was calculated as 159 kJ mol^{-1}, which provided the lower limit for the transition-state energy. We note that the cytosine radical $\boldsymbol{w_1}^\bullet$ was not the lowest-energy neutral fragment, as the ribose-C-4 radical isomer $\boldsymbol{w_1}'^\bullet$ was 30 kJ mol^{-1} more stable (Scheme 4). We did not attempt to computationally locate the transition states and intermediates for the potentially complicated backbone cleavage involving a phosphoester elimination. The fact that the dissociation proceeded to ca. 30% over 150 ms (Figure 1a) indicated an effective rate constant of ca. 2.5 s^{-1}. The dissociation was expected to exhibit a substantial kinetic shift (ΔE_{kin}).[66] Figure 10 shows that the kinetic shift for the **G7rC3a** → **rG78a** isomerization was 233 kJ mol^{-1} to give k_{isom} = 2.5 s^{-1}.

Considering a similar kinetic shift for the dissociation and combining it with the estimated excitation energy from ET (412 kJ mol^{-1}), one can estimate the TS energy for the $\boldsymbol{d_3}$ ion formation at ca. 200 kJ mol^{-1}.

■ CONCLUSIONS

The results of this combined experimental and computational study allow us to arrive at the following conclusions. Stable tetranucleotide DNA cation radicals are formed by electron transfer to dications generated by electrospray ionization. UV–vis photodissociation of the mass-selected cation radicals follows fragmentations that are similar to those induced by collisional activation. This indicates that the excited electronic

Scheme 4. Dissociation of rG78a

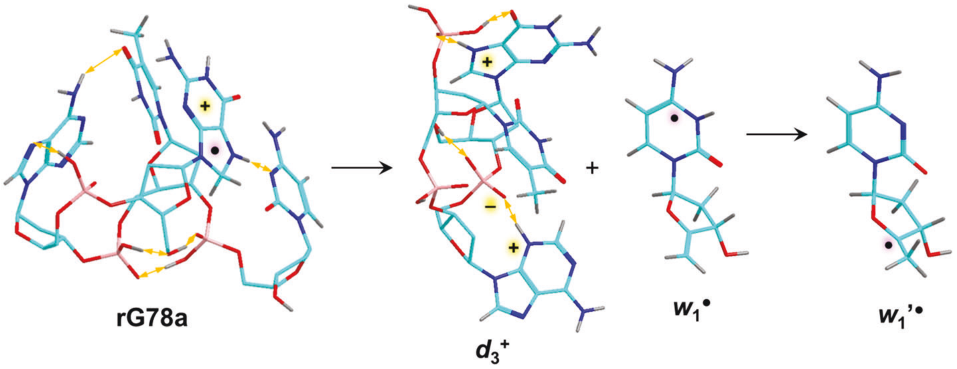

states accessed by photon absorption undergo fast internal conversion to highly excited vibrational states of the ground electronic state. The de-excitation of the cation radicals is probably analogous to the ultrafast internal conversion of excited electronic states in nucleobases, as previously studied by fast spectroscopy in solution. Interpretation of the UV−vis action spectra by TD-DFT vibronic analysis indicated that the cytosine-based radicals that were initially formed by electron transfer underwent fast rearrangement by hydrogen migration, forming low-energy 7,8-dihydroguanine cation radicals. The rearrangement was facilitated by the proximity of the cytosine and guanine nucleobases in the charge-reduced cation radicals and proceeded via a low-energy transition state that was characterized computationally and by reaction kinetics analysis. The present results further indicate that the structure and properties of simpler systems, such as dinucleotide radicals, cannot be readily extrapolated to larger, more complex, oligonucleotides with more intricate networks of intramolecular interactions between the nucleobases. The tetranucleotide cation radicals studied here represent the current limit of size and complexity that is amenable to computational analysis of vibronic UV−vis absorption spectra. Further research with larger DNA oligonucleotide radicals, including those produced from DNA duplexes, is likely to rely on experimental action spectroscopy and empirical assignment of radical-related chromophores.

■ ASSOCIATED CONTENT

Supporting Information

The Supporting Information is available free of charge at https://pubs.acs.org/doi/10.1021/acs.jpcb.0c01693.

Tables of excitation wavelengths and oscillator strengths, electrospray and action spectra of dications, optimized structures, and TD-DFT absorption spectra (PDF)

■ AUTHOR INFORMATION

Corresponding Author

František Tureček − *Department of Chemistry, University of Washington, Seattle, Washington 98195-1700, United States;* orcid.org/0000-0001-7321-7858; Email: turecek@chem.washington.edu

Authors

Shu R. Huang − *Department of Chemistry, University of Washington, Seattle, Washington 98195-1700, United States*

Yue Liu − *Department of Chemistry, University of Washington, Seattle, Washington 98195-1700, United States*

Complete contact information is available at: https://pubs.acs.org/10.1021/acs.jpcb.0c01693

Notes

The authors declare no competing financial interest.

■ ACKNOWLEDGMENTS

Financial support of this research was provided by the Chemistry Division of the U.S. National Science Foundation, grants CHE-1661815 for experimental work and CHE-1624430 for computations. F.T. acknowledges support by the Klaus and Mary Ann Saegebarth Endowment. Thanks are due to Dr. Yang Liu for her help with computer code development.

■ REFERENCES

(1) Kanvah, S.; Joseph, J.; Schuster, G. B.; Barnett, R. N.; Cleveland, C. L.; Landman, U. Oxidation of DNA: Damage to Nucleobases. *Acc. Chem. Res.* **2010**, *43*, 280−287.

(2) Murphy, C. J.; Arkin, M. R.; Jenkins, Y.; Ghatlia, N. D.; Bossmann, S. H.; Turro, N. J.; Barton, J. K. Long-Range Photoinduced Electron-Transfer through a DNA Helix. *Science* **1993**, *262*, 1025−1029.

(3) Giese, B.; Amaudrut, J.; Kohler, A.-K.; Spormann, M.; Wessely, S. Direct Observation of Hole Transfer through DNA by Hopping between Adenine Bases and by Tunneling. *Nature* **2001**, *412*, 318−320.

(4) Shao, F.; Augustyn, K.; Barton, J. K. Sequence Dependence of Charge Transport through DNA Domains. *J. Am. Chem. Soc.* **2005**, *127*, 17445−17452.

(5) Takada, T.; Kawai, K.; Fujitsuka, M.; Majima, T. Direct Observation of Hole Transfer through Double-Helical DNA over 100 A. *Proc. Natl. Acad. Sci. U. S. A.* **2004**, *101*, 14002−14006.

(6) Lewis, F. D.; Daublain, P.; Cohen, B.; Vura-Weis, J.; Wasielewski, M. R. The Influence of Guanine on DNA Hole Transport Efficiency. *Angew. Chem., Int. Ed.* **2008**, *47*, 3798−3800.

(7) Kobayashi, K.; Tagawa, S. Direct Observation of Guanine Radical Cation Deprotonation in Duplex DNA Using Pulse Radiolysis. *J. Am. Chem. Soc.* **2003**, *125*, 10213−10218.

(8) Kobayashi, K.; Yamagami, R.; Tagawa, S. Effect of Base Sequence and Deprotonation of Guanine Cation Radical in DNA. *J. Phys. Chem. B* **2008**, *112*, 10752−10757.

(9) Ghosh, A. K.; Schuster, G. B. Role of the Guanine N1 Imino Proton in the Migration and Reaction of Radical Cations in DNA Oligomers. *J. Am. Chem. Soc.* **2006**, *128*, 4172−4173.

(10) Choi, J.; Tojo, S.; Ahn, D.-S.; Fujitsuka, M.; Miyamoto, S.; Kobayashi, K.; Ihee, H.; Majima, T. Proton Transfer Accompanied by the Oxidation of Adenosine. *Chem. - Eur. J.* **2019**, *25*, 7711−7718.

(11) Choi, J.; Cho, D. W.; Tojo, S.; Fujitsuka, M.; Majima, T. Structural Study of Various Substituted Biphenyls and Their Radical Anions Based on Time-Resolved Resonance Raman Spectroscopy Combined with Pulse Radiolysis. *J. Phys. Chem. A* **2015**, *119*, 851−856.

(12) Kumar, A.; Sevilla, M. D. Influence of Hydration on Proton Transfer in the Guanine-Cytosine Radical Cation ($G^{\bullet +}$-C) Base Pair: A Density Functional Theory Study. *J. Phys. Chem. B* **2009**, *113*, 11359−11361.

(13) Rodriguez-Santiago, L.; Noguera, M.; Bertan, J.; Sodupe, M. Hydrogen Bonding and Proton Transfer in Ionized DNA Base Pairs, Amino Acids and Peptides. In *Quantum Biochemistry*; Matt, C. F., Ed.; Wiley-VCH: Weinheim, Germany, 2010; pp 219−242.

(14) Bertran, J.; Oliva, A.; Rodriguez-Santiago, L.; Sodupe, M. Single versus Double Proton-Transfer Reactions in Watson-Crick Base Pair Radical Cations. A Theoretical Study. *J. Am. Chem. Soc.* **1998**, *120*, 8159−8167.

(15) Colson, A. O.; Besler, B.; Sevilla, M. D. Ab initio Molecular Orbital Calculations on DNA Base Pair Radical Ions: Effect of Base Pairing on Proton-Transfer Energies, Electron Affinities, and Ionization Potentials. *J. Phys. Chem.* **1992**, *96*, 9787−9794.

(16) Hutter, M.; Clark, T. On the Enhanced Stability of the Guanine-Cytosine Base Pair Radical Cation. *J. Am. Chem. Soc.* **1996**, *118*, 7574−7577.

(17) Li, X. F.; Cai, Z. I.; Sevilla, M. D. Investigation of Proton Transfer within DNA Base Pair Anion and Cation Radicals by Density Functional Theory (DFT). *J. Phys. Chem. B* **2001**, *105*, 10115−10123.

(18) Li, X. F.; Cai, Z. I.; Sevilla, M. D. Energetics of the Radical Ions of the AT and AU Base Pairs: A Density Functional Theory (DFT) Study. *J. Phys. Chem. A* **2002**, *106*, 9345−9351.

(19) Feketeova, L.; Chan, B.; Khairallah, G. N.; Steinmetz, V.; Maitre, P.; Radom, L.; O'Hair, R. A. J. Watson-Crick Base Pair Radical Cation as a Model for Oxidative Damage in DNA. *J. Phys. Chem. Lett.* **2017**, *8*, 3159−3165.

(20) Korn, J. A.; Urban, J.; Dang, A.; Nguyen, H. T. H.; Turecek, F. UV-Vis Action Spectroscopy Reveals a Conformational Collapse in

Hydrogen-Rich Dinucleotide Cation Radicals. *J. Phys. Chem. Lett.* **2017**, *8*, 4100−4107.

(21) Liu, Y.; Korn, J. A.; Dang, A.; Turecek, F. Hydrogen-Rich Cation Radicals of DNA Dinucleotides. Generation and Structure Elucidation by UV-Vis Action Spectroscopy. *J. Phys. Chem. B* **2018**, *122*, 9665−9680.

(22) Liu, Y.; Korn, J. A.; Turecek, F. UV-Vis Action Spectroscopy and Structures of Hydrogen-Rich 2′-Deoxycytidine Dinucleotide Cation Radicals. A Difficult Case. *Int. J. Mass Spectrom.* **2019**, *443*, 22−31.

(23) Dang, A.; Korn, J. A.; Gladden, J.; Mozzone, B.; Tureček, F. UV-Vis Photodissociation Action Spectroscopy on Thermo LTQ-XL ETD and Bruker amaZon Ion Trap Mass Spectrometers: A Practical Guide. *J. Am. Soc. Mass Spectrom.* **2019**, *30*, 1558−1564.

(24) Stewart, J. J. P. Optimization of Parameters for Semi-Empirical Methods V: Modification of NDDO Approximations and Applications to 70 Elements. *J. Mol. Model.* **2007**, *13*, 1173−1213.

(25) Řezáč, J.; Fanfrlík, J.; Salahub, D.; Hobza, P. Semi-Empirical Quantum Chemical PM6Method Augmented by Dispersion and H Bonding Correction Terms Reliably Describes Various Types of Noncovalent Complexes. *J. Chem. Theory Comput.* **2009**, *5*, 1749−1760.

(26) Stewart, J. J. P. *MOPAC 16*; Stewart Computational Chemistry: Colorado Springs, CO, 2016.

(27) Řezáč, J. Cuby: An Integrative Framework for Computational Chemistry. *J. Comput. Chem.* **2016**, *37*, 1230−1237.

(28) Berendsen, H. J.; Postma, J. V.; van Gunsteren, W. F.; DiNola, A. R. H. J.; Haak, J. R. Molecular Dynamics with Coupling to an External Bath. *J. Chem. Phys.* **1984**, *81*, 3684−3690.

(29) Becke, A. D. Density-Functional Exchange-Energy Approximation with Correct Asymptotic Behavior. *Phys. Rev. A: At., Mol., Opt. Phys.* **1988**, *38*, 3098−3100.

(30) Chai, J. D.; Head-Gordon, M. Long-Range Corrected Hybrid Density Functionals with Damped Atom-Atom Dispersion Corrections. *Phys. Chem. Chem. Phys.* **2008**, *10*, 6615−6620.

(31) Zhao, Y.; Truhlar, D. G. The M06 Suite of Density Functionals for Main Group Thermochemistry, Thermochemical Kinetics, Noncovalent Interactions, Excited States, and Transition Elements: Two New Functionals and Systematic Testing of Four M06-Class Functionals and 12 Other Functionals. *Theor. Chem. Acc.* **2008**, *120*, 215−241.

(32) Tomasi, J.; Mennucci, B.; Cammi, R. Quantum Mechanical Continuum Solvation Models. *Chem. Rev.* **2005**, *105*, 2999−3093.

(33) Reed, A. E.; Weinstock, R. B.; Weinhold, F. Natural Population Analysis. *J. Chem. Phys.* **1985**, *83*, 735−746.

(34) Dang, A.; Liu, Y.; Tureček, F. UV-Vis Action Spectroscopy of Guanine, 9-Methylguanine and 2′-Deoxyguanosine Cation Radicals in the Gas Phase. *J. Phys. Chem. A* **2019**, *123*, 3272−3284.

(35) Furche, F.; Ahlrichs, A. Adiabatic Time-Dependent Density Functional Methods for Excited State Properties. *J. Chem. Phys.* **2002**, *117*, 7433−7447.

(36) Barbatti, M.; Ruckenbauer, M.; Plasser, F.; Pittner, J.; Granucci, G.; Persico, M.; Lischka, H. Newton-X: A Surface-Hopping Program for Nonadiabatic Molecular Dynamics. *Wiley Interdiscip. Rev.: Comput. Mol. Sci.* **2014**, *4*, 26−33.

(37) Frisch, M. J.; Trucks, G. W.; Schlegel, H. B.; Scuseria, G. E.; Robb, M. A.; Cheeseman, J. R.; Scalmani, G.; Barone, V.; Petersson, G. A.; Nakatsuji, H.; et al. *Gaussian 16*, revision A03; Gaussian, Inc.: Wallingford, CT, 2016.

(38) Gilbert, R. G.; Smith, S. C. *Theory of Unimolecular and Recombination Reactions*; Blackwell Scientific Publications: Oxford, U.K., 1990; pp 52−132.

(39) Zhu, L.; Hase, W. L. *Quantum Chemistry Program Exchange*; Indiana University: Bloomington, IN, 1994; Program no. QCPE 644.

(40) Gregersen, J. A.; Tureček, F. Mass-Spectrometric and Computational Study of Tryptophan Radicals (Trp + H)• Produced by Collisional Electron Transfer to Protonated Tryptophan in the Gas Phase. *Phys. Chem. Chem. Phys.* **2010**, *12*, 13434−13447.

(41) Murray, K. K. DNA Sequencing by Mass Spectrometry. *J. Mass Spectrom.* **1996**, *31*, 1203−1215.

(42) McLuckey, S. A.; Van Berkel, G. J.; Glish, G. L. Tandem Mass Spectrometry of Small, Multiply Charged Oligonucleotides. *J. Am. Soc. Mass Spectrom.* **1992**, *3*, 60−70.

(43) Sapunar, M.; Domcke, W.; Doslic, N. UV Absorption Spectra of DNA Bases in the 350−190 nm Range: Assignment and State Specific Analysis of Solvation Effects. *Phys. Chem. Chem. Phys.* **2019**, *21*, 22782−22793.

(44) Tataurov, A. V.; You, Y.; Owczarzy, R. Predicting Ultraviolet Spectrum of Single Stranded and Double Stranded Deoxyribonucleic Acids. *Biophys. Chem.* **2008**, *133*, 66−70.

(45) Clark, L. B.; Peschel, G. G.; Tinoco, I., Jr. Vapor Spectra and Heat of Vaporization of Some Purine and Pyrimidine Bases. *J. Phys. Chem.* **1965**, *69*, 3615−3618.

(46) Crespo-Hernandez, C. E.; Cohen, B.; Hare, P. M.; Kohler, B. Ultrafast Excited-State Dynamics in Nucleic Acids. *Chem. Rev.* **2004**, *104*, 1977−2020.

(47) Doorley, G. W.; Wojdyla, M.; Watson, G. W.; Towrie, M.; Parker, A. W.; Kelly, J. M.; Quinn, S. J. Tracking DNA Excited States by Picosecond-Time-resolved Infrared Spectroscopy: Signature Band for a Charge-Transfer Excited State in Stacked Adenine-Thymine Systems. *J. Phys. Chem. Lett.* **2013**, *4*, 2739−2744.

(48) Luhrs, D. C.; Viallon, J.; Fischer, I. Excited-State Spectroscopy and Dynamics of Isolated Adenine and 9-Methyladenine. *Phys. Chem. Chem. Phys.* **2001**, *3*, 1827−1831.

(49) Ullrich, S.; Schulz, T.; Zgierski, M. Z.; Stolow, A. Direct Observation of Electronic Relaxation Dynamics in Adenine via Time-Resolved Photoelectron Spectroscopy. *J. Am. Chem. Soc.* **2004**, *126*, 2262−2263.

(50) Kang, H.; Jung, B.; Kim, S. K. Mechanism for Ultrafast Internal Conversion of Adenine. *J. Chem. Phys.* **2003**, *118*, 6717−6719.

(51) Marian, C.; Noliting, D.; Weinkauf, R. The Electronic Spectrum of Protonated Adenine: Theory and Experiment. *Phys. Chem. Chem. Phys.* **2005**, *7*, 3306−3316.

(52) Podolyan, Y.; Gorb, L.; Leszczynski, J. Protonation of Nucleic Acid Bases. A Comprehensive Post-Hartree-Fock Study of the Energetics and Proton Affinities. *J. Phys. Chem. A* **2000**, *104*, 7346−7352.

(53) Colominas, C.; Luque, F. J.; Orozco, M. Tautomerism and Protonation of Guanine and Cytosine. Implications in the Formation of Hydrogen-Bonded Complexes. *J. Am. Chem. Soc.* **1996**, *118*, 6811−6821.

(54) Tureček, F.; Chen, X. Protonated Adenine: Tautomers, Solvated Clusters, and Dissociation Mechanisms. *J. Am. Soc. Mass Spectrom.* **2005**, *16*, 1713−1726.

(55) Hud, N. V.; Morton, T. H. DFT Energy Surfaces for Aminopurine Homodimers ad Their Conjugate Acid Ions. *J. Phys. Chem. A* **2007**, *111*, 3369−3377.

(56) Halder, A.; Bhattacharya, S.; Datta, A.; Bhattacharyya, D.; Mitra, A. The Role of N7 Protonation of Guanine in Determining the Structure, Stability and Function of RNA Base Pairs. *Phys. Chem. Chem. Phys.* **2015**, *17*, 26249−26263.

(57) Wu, R. R.; Yang, B.; Berden, G.; Oomens, J.; Rodgers, M. T. Gas-Phase Conformations and Energetics of Protonated 2-Deoxyguanosine and Guanosine: IRMPD Action Spectroscopy and Theoretical Studies. *J. Phys. Chem. B* **2014**, *118*, 14774−14784.

(58) Yao, C.; Tureček, F.; Polce, M. J.; Wesdemiotis, C. Proton and Hydrogen Atom Adducts to Cytosine. An Experimental and Computational Study. *Int. J. Mass Spectrom.* **2007**, *265*, 106−123.

(59) Filippi, A.; Fraschetti, C.; Rondino, F.; Piccirillo, S.; Steinmetz, V.; Guidoni, L.; Speranza, M. Protonated Pyrimidine Nucleosides Probed by IRMPD Spectroscopy. *Int. J. Mass Spectrom.* **2013**, *354-355*, 54−61.

(60) Salpin, J.-Y.; Guillaumont, S.; Tortajada, J.; MacAleese, L.; Lemaire, J.; Maitre, P. Infrared Spectra of Protonated Uracil, Thymine and Cytosine. *ChemPhysChem* **2007**, *8*, 2235−2244.

(61) Bakker, J. M.; Salpin, J.-Y.; Maitre, P. Tautomerism of Cytosine Probed by Gas Phase IR Spectroscopy. *Int. J. Mass Spectrom.* **2009**, *283*, 214−221.

(62) Lias, S. G.; Bartmess, J. E. Gas-Phase Ion Thermochemistry. In *NIST Chemistry WebBook*; Linstrom, P. J., Mallard, W. G., Eds; NIST Standard Reference Database Number 69; National Institute of Standards and Technology: Gaithersburg, MD, http://webbook.nist.gov (retrieved July 2019).

(63) Hari, Y.; Leumann, C. J.; Schurch, S. What Hinders Electron Transfer Dissociation (ETD) of DNA Cations? *J. Am. Soc. Mass Spectrom.* **2017**, *28*, 2677−2685.

(64) Pepin, R.; Tureček, F. Kinetic Ion Thermometers for Electron Transfer Dissociation. *J. Phys. Chem. B* **2015**, *119*, 2818−2826.

(65) Michl, J. Electronic Spectrum of Fluoranthene. *J. Mol. Spectrosc.* **1969**, *30*, 66−76.

(66) Lifshitz, C. Time-Resolved Appearance Energies, Breakdown Graphs, and Mass Spectra: The Elusive Kinetic Shift. *Mass Spectrom. Rev.* **1982**, *1*, 309−340.